

Valley charge-transfer insulator in twisted double bilayer WSe_2

Received: 27 June 2024

Accepted: 17 January 2025

Published online: 30 January 2025

Check for updates

LingNan Wei^{1,13}, Qingxin Li^{1,13}, Majeed Ur Rehman^{2,13}, Yangchen He³, Dongdong An¹, Shiwei Li¹, Kenji Watanabe⁴, Takashi Taniguchi⁵, Martin Claassen⁶, Kostya S. Novoselov⁷, Dante M. Kennes^{8,9}, Angel Rubio^{9,10}, Daniel A. Rhodes³✉, Ledex Xian^{2,9,11}✉, Geliang Yu^{1,12}✉ & Lei Wang^{1,12}✉

In flat-band systems, emergent physics can be substantially modified by the presence of another nearby electronic band. For example, a Mott–Hubbard insulator can turn into a charge transfer insulator if other electronic states enter between the upper and lower Hubbard bands. Here, we introduce twisted double bilayer (TDB) WSe_2 , with twist angles near 60° , as a controllable platform in which the K -valley band can be tuned to close vicinity of the Γ -valley moiré flat band. At half-filling, correlations split the Γ -valley flat band into upper and lower Hubbard bands and a charge-transfer insulator forms between the Γ -valley upper Hubbard band and K -valley band. Using gate control, we continuously move the K -valley band across the Γ -valley Hubbard bands, and observe a tunable charge-transfer insulator gap and subsequently a continuous phase transition to a metal. The tuning of Mott–Hubbard to charge-transfer insulator establishes valley degree of freedom as a suitable knob for transitions between exotic correlated phases.

Electron transport in solids with a flat dispersion can be dominated by Coulomb interactions if the kinetic energy, set by the bandwidth, is relatively much smaller. From a local Hubbard interaction picture, adding electrons is hindered by the large repulsive Coulomb potential (U) if the band is half-filled, resulting in a Mott–Hubbard insulating state¹. If there is another band nearby, a charge-transfer insulator², with gap Δ defined as the energy between the upper Hubbard band and the second nearby band, will emerge while $\Delta < U$. In this case, excitation no longer hops between adjacent unit cell sites with on-site interaction

energy U , but transfers from the anion to cation atoms within a unit cell with charge-transfer energy Δ , which is determined by the electro-negativity differences between cation and anion. The relative size of U and Δ determines the nature of the insulator and significantly affects emerging phases, like high-temperature superconducting states³. However, traditional charge-transfer insulators usually have complicated band structures and offer little tunability of U , Δ , bandwidth, and carrier density, impeding investigation into the interplay between these parameters and the various resulting correlated phases.

¹National Laboratory of Solid-State Microstructures, Collaborative Innovation Center of Advanced Microstructures, School of Physics, Nanjing University, Nanjing, China. ²Songshan Lake Materials Laboratory, Dongguan, Guangdong, China. ³Department of Materials Science and Engineering, University of Wisconsin, Madison, WI, USA. ⁴Research Center for Electronic and Optical Materials, National Institute for Materials Science, Tsukuba, Japan. ⁵Research Center for Materials Nanoarchitectonics, National Institute for Materials Science, Tsukuba, Japan. ⁶Department of Physics and Astronomy, University of Pennsylvania, Philadelphia, PA, USA. ⁷Department of Materials Science and Engineering, National University of Singapore, Singapore, Singapore. ⁸Institut für Theorie der Statistischen Physik, RWTH Aachen University and JARA-Fundamentals of Future Information Technology, Aachen, Germany. ⁹Max Planck Institute for the Structure and Dynamics of Matter, Center for Free-Electron Laser Science (CFEL), Hamburg, Germany. ¹⁰Center for Computational Quantum Physics, Simons Foundation Flatiron Institute, New York, NY, USA. ¹¹Tsientang Institute for Advanced Study, Hangzhou, Zhejiang, China. ¹²Jiangsu Physical Science Research Center, Nanjing, China. ¹³These authors contributed equally: LingNan Wei, Qingxin Li, Majeed Ur Rehman. ✉e-mail: darhodes@wisc.edu; xianlede@sslslab.org.cn; yugeliang@nju.edu.cn; leiwang@nju.edu.cn

In recent years, two-dimensional (2D) moiré heterostructures have arisen as a potential solution to this problem. 2D moiré heterostructures exhibit great tunability over the carrier density, electronic structure, and have allowed for the exploration of strongly correlated physics⁴, like superconductivity^{5–10}, correlated insulators^{6,11–15}, and anomalous magnetic states^{6,16,17}. In particular, Mott insulators^{15,17–19} and generalized Wigner crystal states^{20,21} have been realized at half or fractional filling of a moiré flat band in twisted transition metal dichalcogenides (TMDs). In this work, we use transport measurement to investigate correlated phases associated with the Γ -valley hole-side moiré flat band in another twisted TMD, TDB-WSe₂. We find that the K -valley, in the absence of electric field, is below the Γ -valley and that its position in energy is highly tunable by a perpendicular electric field. As the Γ -valley moiré flat band splits at half filling, instead of finding a Mott–Hubbard insulator, we observe a correlated phase with a tunable gap, Δ , between the K -valley and the upper Hubbard Γ -valley. Distinct from the conventional charge transfer insulator, where the gap Δ is between anion to cation, the excitation in this new state happens between different valleys. We denote this exotic state of matter as a valley charge-transfer insulator. Intriguingly, we are able to close the gap by tuning the K -valley to be above the Γ -valley at large displacement fields. This allows us to induce a phase transition and to observe a coexistence of a Γ -valley splitting and a K -valley metallic state.

Results

Figure 1 illustrates the dual-gated TDB-WSe₂ device structure. Our stacks were first fabricated by the “pick up and tear” method^{22,23} and then dropped onto pre-patterned, Hall bar-configured, Pt electrodes to achieve good Ohmic contact²⁴ (see method for details). For the twist angle, we choose an angle near 60° so that there is an AA-stacking, twist interface²⁵ between the two inner layers. This allows the band hybridization¹⁸ between layers to dominate near the K point, as opposed to forbidden tunneling due to spin anti-alignment²⁶. In the main text, we focus on one sample with a twist angle of 55.5° (see SI for similar phenomena on more samples with slightly different twist angles). The right panel of Fig. 1a depicts our TDB-WSe₂ lattices in real space, where the hexagon denotes lattice sites where the Γ -valley flat band mainly resides (see Supplementary Fig. 1). Due to the symmetry of the stacking, the Γ -valley flat bands exhibit a relativistic graphene-like dispersion with a Dirac crossing located at the K point of the moiré Brillouin zone²⁵.

Figure 1b shows the schematic band structures of TDB-WSe₂ without (top panel) and with (bottom panel) displacement field (D) as calculated from density functional theory (DFT) (see Supplementary Figs. 1, 2, 3, and 4 in SI). In contrast to twisted bilayer WSe₂^{18,27}, where the Γ -valley flat bands are buried more than 140 meV below the valence band maximum (VBM), due to the stronger interlayer hybridization the Γ -valley flat bands (blue curves) in TDB-WSe₂ rise up to the VBM when

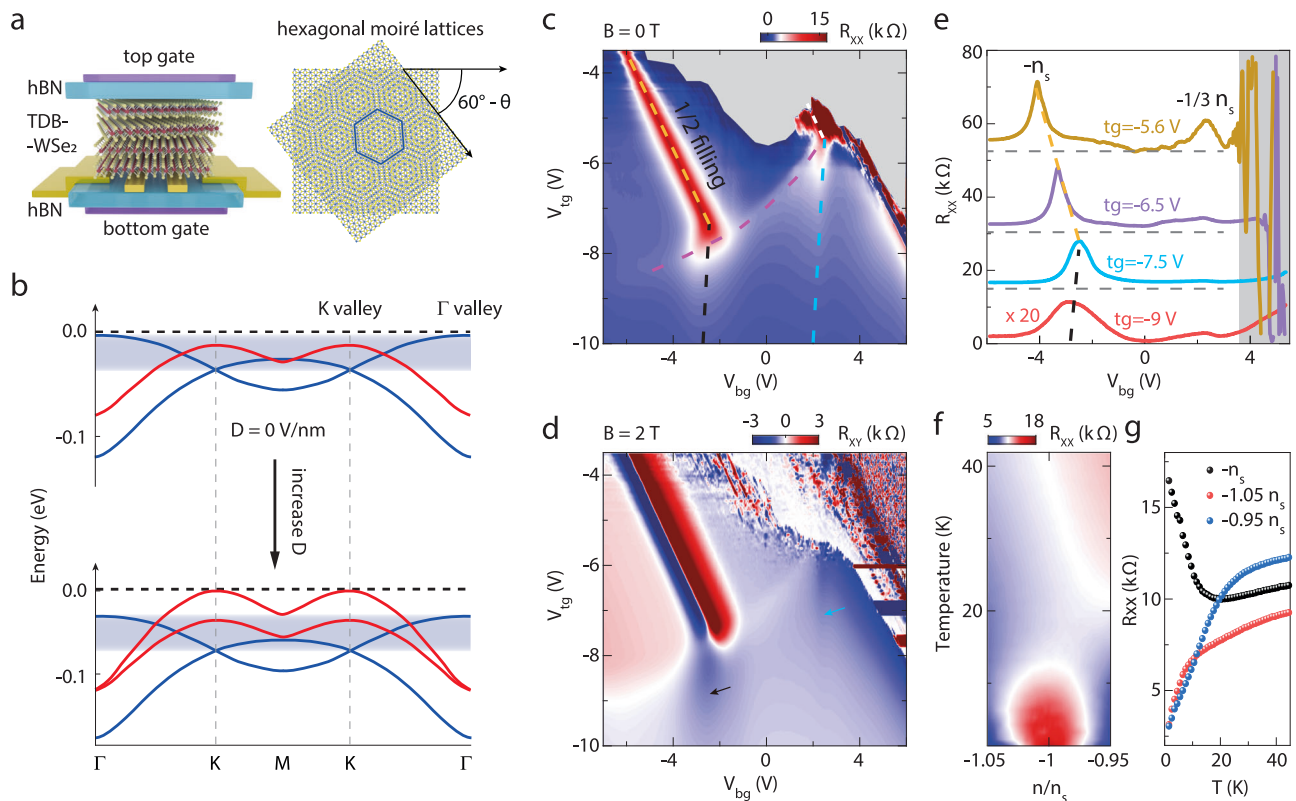


Fig. 1 | Interplay between Γ -valley flat band and K -valley band in TDB-WSe₂. **a** Left: schematic of the device structure. Right: illustration of the moiré pattern TDB-WSe₂ with twist angle $60^\circ - \theta$. **b** Schematic band structures of TDB-WSe₂, based on our DFT results, at a twist angle near 60° without (top) and with (bottom) displacement fields. The blue and red lines represent Γ - and K -valley bands, respectively. The width of the top Γ -valley band, R_{xy} , as a function of V_{tg} and V_{bg} measured at $B = 0$ T and $B = 2$ T, respectively ($T = 1.5$ K). The yellow and black dashed lines trace the evolution of the half-filling correlated insulating states. For **c** the white and blue dashed lines trace the evolution of the $-1/3n_s$ filling states with black and blue arrows pointing to corresponding feature in R_{xy} . The magenta

dashed line highlights a boundary where the K -valley crosses the Fermi level. The gray color in **c** represents the off-region. The corresponding Hall resistances in **(d)** in this off-region are also mainly noise. **e** R_{xx} as a function of V_{bg} at four typical V_{tg} values, which display a half-filling peak at each line and another at $-1/3n_s$ for $V_{tg} = -5.6$ V. The curves are offset for clarity. The horizontal gray dashed lines correspond to zero resistance for each curve. The gray-shaded region on the right side denotes the mobility edges. **f** Map of R_{xx} as a function of temperature and band filling measured at $V_{tg} = -5$ V. **g** R_{xx} as a function of temperature at different band fillings, highlighting the activation of the half-filling correlated insulator and the metallic behavior at densities away from half-filling.

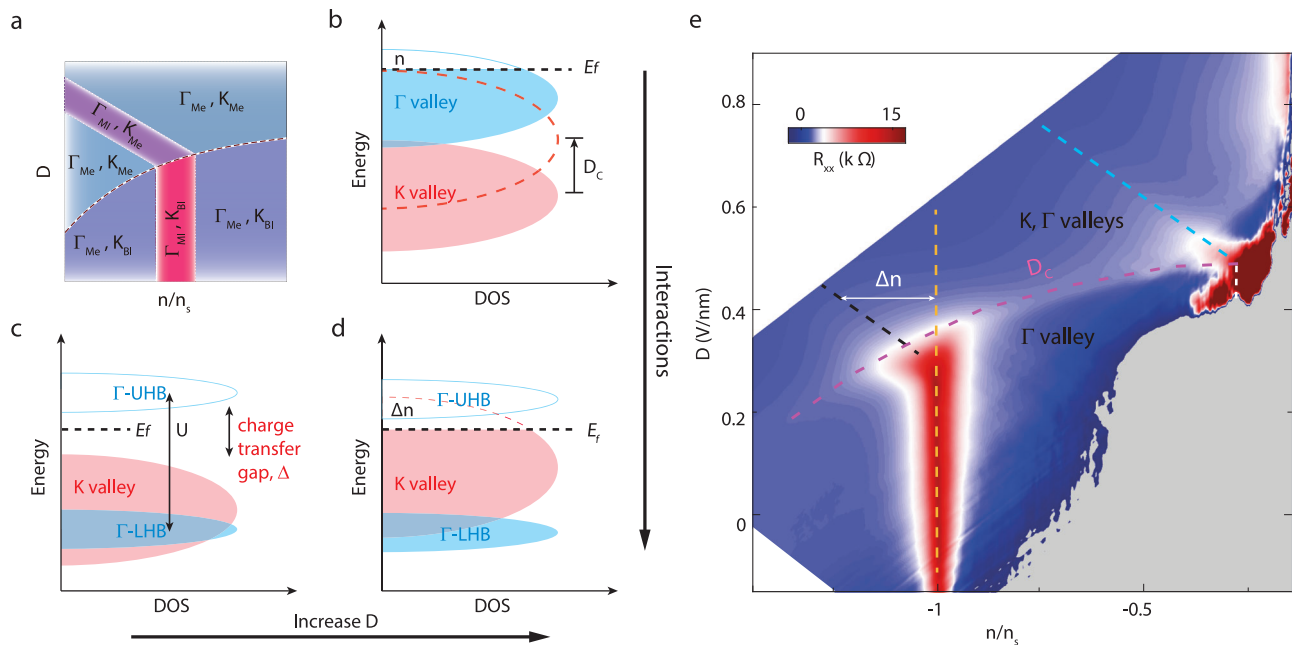


Fig. 2 | Displacement field and doping response of the correlated phases in TDB-WSe₂. **a** Schematic phase diagram of TDB-WSe₂ resulting from the theoretical model in **(b–d)**. Here, Γ_x and K_x denote the nature of the corresponding bands with $x = \text{Me}$, $x = \text{MI}$, and $x = \text{BI}$ denoting metallic, Mott-Hubbard insulating and band insulating states, respectively. **b** Single particle band illustration: at a carrier concentration n ($n/n_s \neq -1$), the upper edge of the K -valley band touches the Fermi level when $D = D_c$. In a single particle picture, for $D < D_c$, only Γ -valley is filled; and for

$D > D_c$, both K -valley and Γ -valley are filled. **c, d** At half-filling, $n/n_s = -1$, the Γ -valley flat band splits into the upper and lower Hubbard band via strong Coulomb interaction. **c** and **d** correspond to the sample under a small and large D , respectively. **e** Resistance versus displacement field and band filling, replotted from the same dataset in Fig. 1c all the dashed lines follow the same coloring definition as in Fig. 1c gray color represents the off region and white color represents the regions not measured.

$D = 0$ V/nm. Moreover, the Γ - and the K -valley bands are very close in energy with considerable overlaps, but hybridization between these two bands remains small because the two are rooted in different atomic orbitals of the metal and chalcogen atoms²⁵. With increasing D , the K -valley bands (red curves) split, and the VBM shifts to one of the K -valley bands, while the Γ -valley flat bands remain almost unaffected. These unique features of the electronic band structure, induced by the moiré potential, allow us to study the interplay between correlated states in the Γ -valley flat band and K -valley states.

To begin investigating this interplay, we first measure R_{xx} ($B = 0$ T) and R_{xy} ($B = 2$ T) while sweeping the top (V_{tg}) and bottom (V_{bg}) gates, Fig. 1c, d. A prominent resistive peak in R_{xx} , marked by the yellow dashed line, is observed along the constant half-filling density, which we denote as $-n_s$, corresponding to one hole per moiré unit cell. The R_{xy} around this feature changes sign three times, indicating a correlated insulating state that deviates strongly from the single-particle band structure¹⁸. Tracing the $n/n_s = -1$ peak to larger negative V_{tg} values, the resistance first gradually decreases (up to $V_{tg} \approx -8$ V), and then quickly collapses to a small residual resistance peak traced by the black dashed line. The R_{xy} in this region, black arrow Fig. 1d, exhibits slightly higher values than the background, but without sign change. Similar dependence also appears at $-1/3n_s$ filling, marked by white and blue dashed lines. This trend is highlighted in the R_{xx} versus V_{bg} curves under four different V_{tg} values from -5.6 V to -9 V in Fig. 1e.

To further verify the correlated insulating nature of the state at half-filling, we show the temperature dependence of R_{xx} near this doping regime in Fig. 1f, g. Above a critical temperature, $T_C \approx 12$ K, the sample shows a metallic behavior. Below T_C , as the sample is cooled the resistance at half-filling increases in a manner consistent with a thermally activated insulator. When it is doped slightly away from half-filling, the insulating behavior changes to metallic. Intriguingly, we also observe a small resistance peak (magenta dashed line, Fig. 1c) which intersects with both the $n/n_s = -1$ and $-1/3$ insulating states at their

transition points. We have measured similar phenomena in other devices with similar twist angles (Supplementary Fig. 5). We hypothesize that this feature is related to an evolution of the band structure, which may destroy the correlated state.

Following this hypothesis, we draw a cartoon phase diagram of the gate-gate behavior in terms of D and the band filling (n/n_s) in Fig. 2a. Our reasoning for this model is as follows: first we consider the system without electron interactions in (Fig. 2b) under zero and finite D . As shown in Fig. 1b, D has little effect on the Γ -valley band but can significantly broaden the K -valley bandwidth and shift its position in energy upwards. At a critical displacement field, D_c , the K -valley (red dashed line, Fig. 2b) reaches the Fermi level, whose position also determines the doping density n . When n is lower (higher), the Fermi level is further from (closer to) the K -valley band and thus there is a larger (smaller) resulting D_c , explaining the phase boundary defined by the $D = D_c$ line in Fig. 2a. In this picture when $D < D_c$ only the Γ -valley will be filled. However, when $D > D_c$, carriers will reside in both the Γ - and K -valleys.

Next, we consider what happens when we add Coulomb interactions into the model (Fig. 2c). At half-filling, the Γ flat band splits into lower (LHB) and upper (UHB) Hubbard bands. Because the difference in energy between the Γ - and K -valleys (from DFT, see SI) is small, the LHB lies below the K -valley band. As a consequence, a charge-transfer insulator with a gap Δ smaller than U is formed between the K -valley maximum and the UHB minimum. Thus we assign this gap as a correlated insulating state, where D can continuously tune the size of Δ all the way to zero. Experimentally, we observe the results of this model as we tune from the insulating state ($D < D_c$) to the metallic state ($D = D_c$) where the K -valley touches the UHB and closes the gap (intersection of the yellow and magenta dashed lines in Fig. 2e).

Finally, in Fig. 2d, we examine what happens to the correlated insulating states when the K -valley begins to overlap with the UHB (i.e., $D > D_c$). As a result of this overlap, additional Δn carriers are needed to

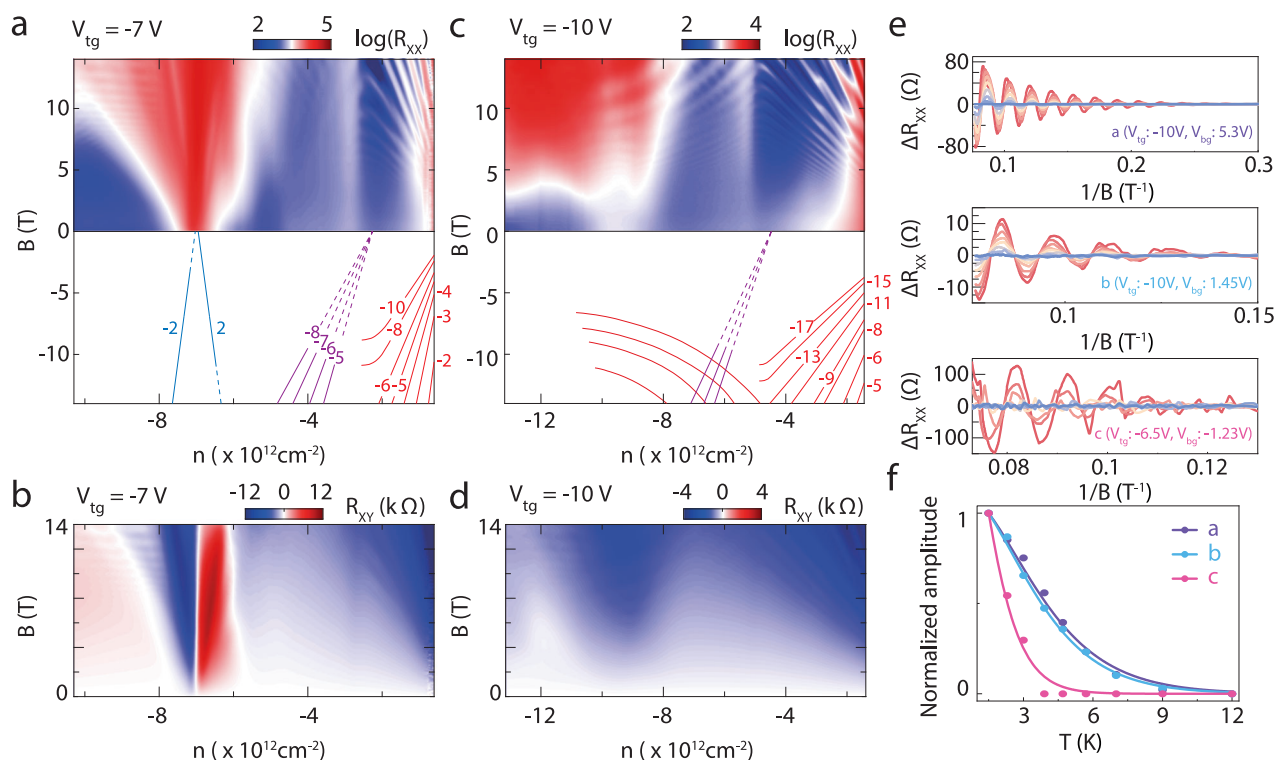


Fig. 3 | Magneto-transport on the K - and Γ -valley bands in TDB-WSe₂. **a, b** R_{xx} and R_{xy} as a function of carrier density, n , and magnetic field, B , at $V_{tg} = -7$ V ($T = 1.5$ K). **c, d** R_{xx} and R_{xy} versus n and B at $V_{tg} = -10$ V (1.5 K). **e** Temperature-dependent quantum oscillations ΔR_{xx} versus $1/B$ at three representative positions.

From red to blue, the temperatures are 1.5, 2.3, 3, 3.9, 4.7, 5.7, 7, 9, and 12 K. **f** Normalized amplitude versus T for three representative points: **(a, b, c)**. Solid lines fit the Lifshitz–Kosevich formula.

fill the K -valley in order to keep the Γ -valley band at half-filling. Intuitively, a larger D will shift the K -valley further up in energy and will result in a larger Δn . With this understanding in mind, we look back on Fig. 1c and re-plot it as a function of D and (n/n_s) in Fig. 2e with the same colored dashed lines as in Fig. 1c marking the main features. In agreement with the theoretical phase diagram (Fig. 2b), we find a critical value of D , D_c , above which the resistance of the correlated states at $n = -n_s$ and $-1/3n_s$ will collapse. The correlated behavior, marked by a black line in Fig. 2e, corresponds to the Γ -valley band being in the Mott “Hubbard state concomitant with the K -valley band being in a metallic state, as suggested by Fig. 2d. Because the two bands overlap in energy, the behavior observed in electronic transport is metallic (see temperature dependence in Supplementary Fig. 6). Similarly, the correlated insulating state seen at $-1/3n_s$ filling also diminishes to small resistance peaks, marked by the dashed blue line in Fig. 2e.

To further prove the validity of the phase diagram presented in Fig. 2a and the existence of a charge-transfer insulator state, we examine the sample under perpendicular magnetic fields. Figure 3a, b shows the R_{xx} and R_{xy} values versus n and B up to 14 T with V_{tg} fixed at -7 V (see Supplementary Figs. 7 and 8 for other values of V_{tg} and similar behavior in another device). With sweeping V_{bg} , the constant $V_{tg} = -7$ V line crosses the magenta dashed line in Fig. 1c. As a result, in the low-doping region D is much larger than D_c and the K -valley band is at the VBM. So the observed Landau fan (red lines, Fig. 3a) originates from the K -valley band edge. Starting from the lowest Landau level -2 , both odd and even-integer quantum Hall states are observed, suggesting a full lifting of the spin-valley degeneracy. As we move to higher carrier density, we observe a second set of Landau fans (purple lines) whose trajectories point towards the Γ -valley band edge. Different from the Mott insulator phase in $tbWSe_2$ ¹⁸, we find that the charge-transfer

insulator peak (located at $n \sim 7 \times 10^{12} \text{ cm}^{-2}$) in TDB-WSe₂ survives up to 14 T.

Upon increasing D further by fixing V_{tg} at -10 V (Fig. 3c, d), we enter the $D > D_c$ region where only the correlated metallic state is observed. This state exists up to high magnetic field without sign change in the corresponding R_{xy} . Similar to $V_{tg} = -7$ V, as a result of the sample residing in the $D > D_c$ region, we observe two sets of Landau fans originating from the Γ and K -valley bands. As compared to $V_{tg} = -7$ V, we also observe that the separation in carrier density between these two sets of Landau fans increases, in agreement with the predicted shift of the K -valley band from DFT. Notice that there is a set of curved Landau fans, which cross the correlated metallic state and may be pointing toward full filling of the K -valley. We speculate that the slope of these fans is affected by the simultaneous filling of the Γ -valley band. To further confirm the origin of the Landau fans, we extract the effective mass of each region by measuring the temperature-dependent SdH oscillations (Fig. 3e) at three fixed V_{tg} and V_{bg} values, marked as a, b, and c. To determine the effective mass, we used the Lifshitz–Kosevich formula $A(T) = A_0 \frac{2\pi^2 k_B T / \hbar \omega_c}{\sinh(2\pi^2 k_B T / \hbar \omega_c)}$, where $A_0 = 4 \exp(-2\pi^2 k_B T_D / \hbar \omega_c)$, $\omega_c = eB / m^* c$ is the cyclotron frequency, $T_D = \hbar / 2\pi k_B \tau_q$ is the Dingle temperature, \hbar is the reduced Planck’s constant, and k_B is the Boltzmann constant. Figure 3f shows the normalized amplitude versus temperature at a, b, and c. Indeed, the fits show that the effective masses at a and b, associated with the K -valley fans, are lighter ($0.39m_e$ and $0.52m_e$, m_e is the bare electron mass) while the effective mass at c, related to the Γ valley fans, is heavier ($1.14m_e$), as expected from theory.

Finally, we investigate the displacement field-induced metal-insulator phase transition of the charge-transfer insulator. Figure 4a

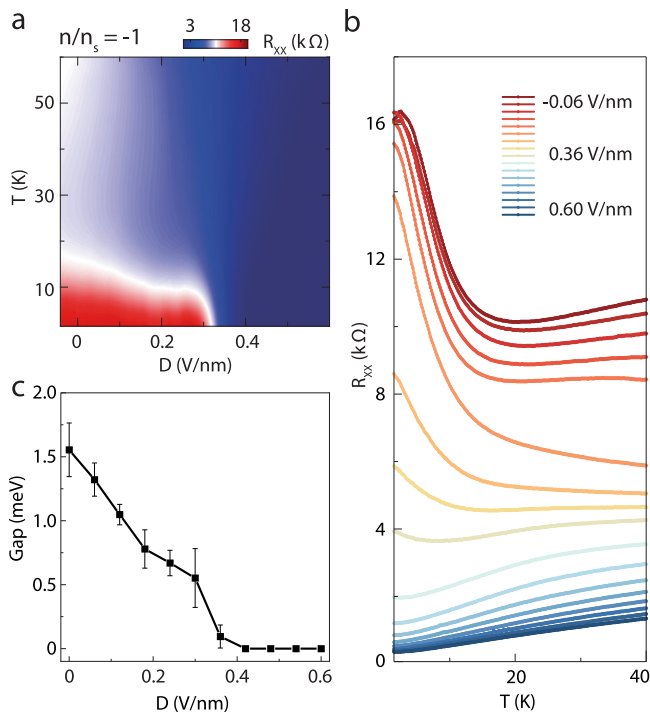


Fig. 4 | Displacement field tunable charge-transfer insulator gap and insulator-metal phase transition in TDB-WSe₂. **a** R_{xx} as a function of D and T at $n/n_s = -1$. **b** R_{xx} versus T curves for D ranging from -0.06 V/nm to 0.6 V/nm. The $R_{xx} - T$ dependence changes smoothly from insulating to metallic behavior with D at low T . **c** Δ versus displacement field at $n/n_s = -1$. Error bars reflect the uncertainty in determining the linear region for the fit.

displays the resistance along the constant half-filling line versus D and temperature. It unambiguously shows an insulator-metal phase boundary around $D = 0.38$ V/nm (for similar transitions in other devices, see Supplementary Fig. 9). In Fig. 4b, we plot a series of $R-T$ curves below and above the phase boundary in Fig. 4a. The curves for D values ranging from -0.06 V/nm to 0.36 V/nm exhibit an insulating behavior at temperature below 12 K, with resistances increasing with decreasing temperature. This behavior becomes weaker with increasing D , up to 0.36 V/nm where the $R-T$ curve is nearly flat. Upon further increasing of D from 0.4 V/nm to 0.6 V/nm, we see a smooth transition from an insulating state to a metallic one. To quantify this change, we extract the activation gap Δ for each curve in Fig. 4c (see fittings in Supplementary Fig. 10). We observe a maximum gap size of 1.8 meV at $D = 0$, which decreases monotonically with increasing D until $D = 0.4$ V/nm, where the metallic states from the K -valley band dominate the transport behavior. Although a phase transition from a Mott insulator state to a metallic state has been theoretically and experimentally reported in twisted TMDs^{28–31}, the mechanism is due to the increasing bandwidth of the moiré flat band under finite D . However, for TDB-WSe₂, small D does not change the F -valley bandwidth and, therefore, we attribute this tunable gap to the rising of the K -valley, in accordance with our theoretical model discussed in Fig. 2. Thus we have demonstrated a tunable phenomena in moiré heterostructures: a charge-transfer gap in TDB-WSe₂, where a phase transition at $n/n_s = -1$ is induced by D and the result of this gap closing between the F flat band and the K -valley band.

Discussion

Going beyond the established moiré control paradigm of tuning bandwidths, our work establishes an additional control knob—the valley degree of freedom. With this, we demonstrate valley-enabled

control of many-body phases of matter, including correlated Mott-Hubbard and charge transfer states. The continuous control of phase transitions between different correlated states and metals using purely displacement fields is a unique application of this valley-enabled control. This phenomenon elevates TDB-WSe₂, and similar TMD structures, as novel platforms significantly expand on the available moiré materials engineering. Owing to the widely tunable band structure, TDB-TMDs can provide model systems to systematically explore other emergent electronic phases, such as the realization of correlated insulators as potential parent states to unconventional superconductors (analogous to charge-transfer cuprates³), exciton condensates, and potentially even spin-liquid states³².

Methods

Sample fabrication

We used the pick-up transfer method²² to fabricate the twisted double bilayer WSe₂ (TDB-WSe₂) devices. All the flakes including bilayer WSe₂, hexagonal boron nitride (hBN), and few-layer graphite were mechanically exfoliated from the bulk crystal on Si substrates with a 285 nm oxide layer. We fabricated prepatterned leads by first preparing a stack of hBN/Graphite as the bottom gate, and then evaporating a Hall-bar-shaped Cr/Pt (1/20 nm) metallic leads on the hBN layer. To fabricate the twisted TDB-WSe₂ stack, we picked up another hBN (25–50 nm) flake and used it to pick up the TDB-WSe₂ flakes by the “pick up and tear” method^{22,23}. The hBN/TDB-WSe₂ stack was then dropped onto the pre-patterned Pt leads. Lastly, a metal top gate was evaporated on the top layer h-BN.

DFT calculation on the bandstructure

In order to assess the electronic properties of TDB-WSe₂ system, we performed the first principle calculations based on density functional theory (DFT) as implemented in the Vienna ab initio simulation package (VASP)³³. The pseudo-potentials approach under the framework of the projected augmented-wave method (PAW) was used to perform the first principal Ab initio calculations³⁴. Plane-wave basis sets with cutoff energy equal to 500 eV were employed. The generalized gradient approximation (GGA) under the Perdew-Burke-Ernzerhof (PBE) scheme was used to model the exchange-correlation interaction³⁵. Due to the large size of the moiré supercells, only the Γ point was considered in all the self-consistent calculations. A slab model was used with vacuum thickness more than 15 Å to avoid the artificial interaction between the periodic slabs. To cover the Van der Waals interaction between the adjacent layers, Tkatchenko-Scheffler method was applied during the relaxation³⁶. All the structures were fully relaxed until the largest Hellmann Feynman force on each atom converged to values smaller than 0.01 eV/Å. For figures like charge density distributions and atomic structure visualization, we used the VESTA code³⁷.

To model the TDB-WSe₂ systems, we placed the bilayer WSe₂ over the bilayer WSe₂ with twisted angles between the constituent bilayer WSe₂ to be $(60 - \theta)$ degrees. In our work, we specifically focused on the systems with $\theta = 5.08^\circ$ and 4.4° . Extensive DFT calculations were performed both in the absence and presence of displacement fields. Spin-orbit interactions were included in all the calculations.

Data availability

The data that support the findings of this study are available from the corresponding authors upon request.

Code availability

The code that supports the findings of this study is available from the corresponding authors upon request.

References

- Mott, N. F. Metal-insulator transition. *Rev. Mod. Phys.* **40**, 677 (1968).
- Zaanen, J., Sawatzky, G. & Allen, J. Band gaps and electronic structure of transition-metal compounds. *Phys. Rev. Lett.* **55**, 418 (1985).
- Zhang, F. & Rice, T. Effective Hamiltonian for the superconducting Cu oxides. *Phys. Rev. B* **37**, 3759 (1988).
- Kennes, D. M. et al. Moiré heterostructures as a condensed-matter quantum simulator. *Nat. Phys.* **17**, 155–163 (2021).
- Cao, Y. et al. Unconventional superconductivity in magic-angle graphene superlattices. *Nature* **556**, 43–50 (2018).
- Lu, X. et al. Superconductors, orbital magnets, and correlated states in magic-angle bilayer graphene. *Nature* **574**, 653–657 (2019).
- Park, J. M., Cao, Y., Watanabe, K., Taniguchi, T. & Jarillo-Herrero, P. Tunable strongly coupled superconductivity in magic-angle twisted trilayer graphene. *Nature* **590**, 249–255 (2021).
- Hao, Z. et al. Electric field-tunable superconductivity in alternating-twist magic-angle trilayer graphene. *Science* **371**, 1133–1138 (2021).
- Oh, M. et al. Evidence for unconventional superconductivity in twisted bilayer graphene. *Nature* **600**, 240–245 (2021).
- Fischer, A. et al. Unconventional superconductivity in magic-angle twisted trilayer graphene. *npj Quantum Mater.* **7**, 1–10 (2022).
- Cao, Y. et al. Correlated insulator behaviour at half-filling in magic-angle graphene superlattices. *Nature* **556**, 80–84 (2018).
- Burg, G. W. et al. Correlated insulating states in twisted double bilayer graphene. *Phys. Rev. Lett.* **123**, 197702 (2019).
- Choi, Y. et al. Interaction-driven band flattening and correlated phases in twisted bilayer graphene. *Nat. Phys.* **17**, 1375–1381 (2021).
- Xu, S. et al. Tunable van Hove singularities and correlated states in twisted monolayer–bilayer graphene. *Nat. Phys.* **17**, 619–626 (2021).
- Shimazaki, Y. et al. Strongly correlated electrons and hybrid excitons in a moiré heterostructure. *Nature* **580**, 472–477 (2020).
- Sharpe, A. L. et al. Emergent ferromagnetism near three-quarters filling in twisted bilayer graphene. *Science* **365**, 605–608 (2019).
- Li, T. et al. Quantum anomalous Hall effect from intertwined moiré bands. *Nature* **600**, 641–646 (2021).
- Wang, L. et al. Correlated electronic phases in twisted bilayer transition metal dichalcogenides. *Nat. Mater.* **19**, 861–866 (2020).
- Li, T. et al. Charge-order-enhanced capacitance in semiconductor moiré superlattices. *Nat. Nanotechnol.* **16**, 1068–1072 (2021).
- Miao, S. et al. Strong interaction between interlayer excitons and correlated electrons in WSe₂/WS₂ moiré superlattice. *Nat. Commun.* **12**, 3608 (2021).
- Regan, E. C. et al. Mott and generalized Wigner crystal states in WSe₂/WS₂ moiré superlattices. *Nature* **579**, 359–363 (2020).
- Wang, L. et al. One-dimensional electrical contact to a two-dimensional material. *Science* **342**, 614–617 (2013).
- Kim, K. et al. van der Waals heterostructures with high accuracy rotational alignment. *Nano Lett.* **16**, 1989–1995 (2016).
- Movva, H. C. et al. High-mobility holes in dual-gated WSe₂ field-effect transistors. *ACS Nano* **9**, 10402–10410 (2015).
- Xian, L. et al. Realization of nearly dispersionless bands with strong orbital anisotropy from destructive interference in twisted bilayer mos₂. *Nat. Commun.* **12**, 5644 (2021).
- Xu, Y. et al. A tunable bilayer Hubbard model in twisted WSe₂. *Nat. Nanotechnol.* **17**, 934–939 (2022).
- Zhang, Z. et al. Flat bands in twisted bilayer transition metal dichalcogenides. *Nat. Phys.* **16**, 1093–1096 (2020).
- Morales-Durán, N., MacDonald, A. H. & Potasz, P. Metal-insulator transition in transition metal dichalcogenide heterobilayer moiré superlattices. *Phys. Rev. B* **103**, L24110 (2021).
- Pan, H. & Sarma, S. D. Interaction-driven filling-induced metal-insulator transitions in 2D moiré lattices. *Phys. Rev. Lett.* **127**, 096802 (2021).
- Ghiotto, A. et al. Quantum criticality in twisted transition metal dichalcogenides. *Nature* **597**, 345–349 (2021).
- Li, T. et al. Continuous Mott transition in semiconductor moiré superlattices. *Nature* **597**, 350–354 (2021).
- Motruk, J., Rossi, D., Abanin, D. A. & Rademaker, L. Kagome chiral spin liquid in transition metal dichalcogenide moiré bilayers. *Phys. Rev. Res.* **5**, L022049 (2023).
- Kresse, G. & Furthmüller, J. Efficient iterative schemes for ab initio total-energy calculations using a plane-wave basis set. *Phys. Rev. B* **54**, 11169 (1996).
- Blöchl, P. E. Projector augmented-wave method. *Phys. Rev. B* **50**, 17953 (1994).
- Perdew, J. P., Burke, K. & Ernzerhof, M. Generalized gradient approximation made simple. *Phys. Rev. Lett.* **77**, 3865 (1996).
- Tkatchenko, A. & Scheffler, M. Accurate molecular van der Waals interactions from ground-state electron density and free-atom reference data. *Phys. Rev. Lett.* **102**, 073005 (2009).
- Momma, K. & Izumi, F. Vesta 3 for three-dimensional visualization of crystal, volumetric and morphology data. *J. Appl. Crystallogr.* **44**, 1272–1276 (2011).

Acknowledgements

L.W. acknowledges the National Key Projects for Research and Development of China (Grant No. 2022YFA1200141 and 2021YFA1400400), National Natural Science Foundation of China (Grant No. 12074173), Natural Science Foundation of Jiangsu Province (Grant No. BK20220066 and BK20233001), Program for Innovative Talents and Entrepreneur in Jiangsu (Grant No. JSSCTD202101) and Nanjing University International Research Seed Fund. D.M.K. acknowledge funding by the Deutsche Forschungsgemeinschaft (DFG, German Research Foundation) under RTG 1995 and within the Priority Program SPP 2244 “2DMP”—443273985. G.Y. acknowledges the helpful discussions with Shijun Li, Jiangsu Feynman Tech Group and the financial support from the National Key R&D Program of China (Nos. 2024YFB3715405 and Nos. 2022YFA120470). L.X. and M.U.R. acknowledge the support by the National Key Research and Development Program of China (Grant No. 2022YFA1403501), Guangdong Basic and Applied Basic Research Foundation (Grant No. 2022B1515120020), and the National Natural Science Foundation of China (Grant No. 62341404), Hangzhou Tsien-tang Education Foundation and the Max Planck Partner group program. The computational resources were provided by the Platform for Data-Driven Computational Materials Discovery of the Songshan Lake Materials Laboratory. M.U.R. acknowledges the support by National Natural Science Foundation of China (Grant No. 12350410367). K.W. and T.T. acknowledge support from the JSPS KAKENHI (Grant Numbers 21H05233 and 23H02052) and World Premier International Research Center Initiative (WPI), MEXT, Japan. A.R. acknowledges the support by the European Research Council (ERC-2015-AdG-694097), Grupos Consolidados (IT1249-19), SFB925, and by the Deutsche Forschungsgemeinschaft (DFG, German Research Foundation) under Germany’s Excellence Strategy—Cluster of Excellence and Advanced Imaging of Matter (AIM) EXC 2056 - 390715994 and RTG 2247. M.C. is supported by a startup grant from the University of Pennsylvania. A.R. is supported by the Flatiron Institute, a division of the Simons Foundation. D.A.R. and Y.H. acknowledge support from the University of Wisconsin-Madison, Office of the Vice Chancellor for Research and Graduate Education with funding from the Wisconsin Alumni Research Foundation.

Author contributions

L.W. conceived and supervised the experiment. L.N.W., Q.L., D.A., and S.L. fabricated the samples. L.N.W. performed the transport measurements. D.M.K., L.X., L.N.W., and L.W. analyzed the data. D.A.R. and Y.H. grew the WSe₂ crystals. K.W. and T.T. supplied the hBN crystals. M.U.R. and L.X. performed the density functional theory calculations. L.X.,

D.M.K., M.C., and A.R. supervised the theoretical aspects of this work. L.N.W. and L.W. wrote the manuscript with input from D.A.R., L.X., D.M.K., K.S.N. and G.Y.

Competing interests

The authors declare no competing interests.

Additional information

Supplementary information The online version contains supplementary material available at <https://doi.org/10.1038/s41467-025-56490-w>.

Correspondence and requests for materials should be addressed to Daniel A. Rhodes, Ledex Xian, Geliang Yu or Lei Wang.

Peer review information *Nature Communications* thanks the anonymous, reviewer(s) for their contribution to the peer review of this work. A peer review file is available.

Reprints and permissions information is available at <http://www.nature.com/reprints>

Publisher's note Springer Nature remains neutral with regard to jurisdictional claims in published maps and institutional affiliations.

Open Access This article is licensed under a Creative Commons Attribution-NonCommercial-NoDerivatives 4.0 International License, which permits any non-commercial use, sharing, distribution and reproduction in any medium or format, as long as you give appropriate credit to the original author(s) and the source, provide a link to the Creative Commons licence, and indicate if you modified the licensed material. You do not have permission under this licence to share adapted material derived from this article or parts of it. The images or other third party material in this article are included in the article's Creative Commons licence, unless indicated otherwise in a credit line to the material. If material is not included in the article's Creative Commons licence and your intended use is not permitted by statutory regulation or exceeds the permitted use, you will need to obtain permission directly from the copyright holder. To view a copy of this licence, visit <http://creativecommons.org/licenses/by-nc-nd/4.0/>.

© The Author(s) 2025